magnetochemistry

MDPI

Article

Superparamagnetism of Baked Clays Containing Polymorphs of Iron Oxides: Experimental Study and Theoretical Modeling

Petr Kharitonskii [1,2], Andrei Krasilin [2], Nadezhda Belskaya [2], Svetlana Yanson [3], Nikita Bobrov [3], Andrey Ralin [4], Kamil Gareev [2,5,*], Nikita Zolotov [6], Dmitry Zaytsev [7] and Elena Sergienko [2,3]

1 Department of Physics, Saint Petersburg Electrotechnical University "LETI", 197022 Saint Petersburg, Russia; peterkh@yandex.ru
2 Ioffe Institute, Russian Academy of Sciences, 194021 Saint Petersburg, Russia; ikrasilin@mail.ioffe.ru (A.K.); nadejda-bels@mail.ru (N.B.); e.sergienko@spbu.ru (E.S.)
3 Department of Earth Physics, Saint Petersburg State University, 199034 Saint Petersburg, Russia; svetlana.janson@spbu.ru (S.Y.); nbobrov@bk.ru (N.B.)
4 Institute of Mathematics and Computer Technologies, Far Eastern Federal University, 690922 Vladivostok, Russia; ralin.ayu@dvfu.ru
5 Department of Micro and Nanoelectronics, Saint Petersburg Electrotechnical University "LETI", 197022 Saint Petersburg, Russia
6 SemiTEq JSC, 194156 Saint Petersburg, Russia; nikita13300@yandex.ru
7 Institute of Earth Sciences, Saint Petersburg State University, 199034 Saint Petersburg, Russia; st096199@student.spbu.ru
* Correspondence: kggareev@etu.ru

Abstract

A comprehensive study of the magnetic properties of baked clays containing ferrimagnetic particles in various magnetic states, including superparamagnetic, has been carried out in this work. The phase composition of the magnetic fraction of laboratory and industrial samples made from the same clay is mainly represented by iron (III) oxide polymorphs and possibly non-stoichiometric magnetite. Experimental methods included magnetic granulometry, Mössbauer spectroscopy, scanning electron microscopy, X-ray phase analysis, and pulsed electromagnetic measurements. A theoretical model of magnetostatically interacting particles with a lognormal volume distribution was used to interpret the experimental data, allowing the contribution of superparamagnetic grains to be taken into consideration. It is shown that the firing mode significantly affects the composition of iron oxide phases and their magnetic characteristics. Laboratory samples are characterized by approximately twice the proportion of superparamagnetic particles. At sufficiently low concentrations of ferrimagnet in samples <0.1%, the concentration of superparamagnetic particles is even two orders of magnitude lower. It is the use of pulse methods that provides a more reliable diagnosis of their presence. The complex application of experimental methods with theoretical modeling makes it possible to reveal and quantitatively describe the microheterogeneous nature of the magnetic state of baked clays, which is applicable to a wide range of magnetic materials, and to analyze more deeply the thermal and phase history of archaeological and geological objects.

Keywords: superparamagnetism; polymorphs of iron oxides; baked clays; bricks; blocking volume; magnetostatic interaction; magnetic susceptibility; frequency dependence factor; hysteresis characteristics; magnetic granulometry

check for updates

Academic Editor: Evgeny Katz

Received: 5 October 2025
Revised: 15 November 2025
Accepted: 22 November 2025
Published: 25 November 2025

Citation: Kharitonskii, P.; Krasilin, A.; Belskaya, N.; Yanson, S.; Bobrov, N.; Ralin, A.; Gareev, K.; Zolotov, N.; Zaytsev, D.; Sergienko, E. Superparamagnetism of Baked Clays Containing Polymorphs of Iron Oxides: Experimental Study and Theoretical Modeling. *Magnetochemistry* **2025**, *11*, 103. https://doi.org/10.3390/magnetochemistry11120103

Copyright: © 2025 by the authors. Licensee MDPI, Basel, Switzerland. This article is an open access article distributed under the terms and conditions of the Creative Commons Attribution (CC BY) license (https://creativecommons.org/licenses/by/4.0/).

1. Introduction

Superparamagnetic nanoparticles of iron and its oxides represent an important object of research in geophysics, ecology, and materials science. They are widely distributed in soils, loesses, and sedimentary rocks, where they can serve as indicators of paleoecological conditions [1–3]. Fired clays are particularly relevant: their magnetic properties record the temperature history of thermal processes and can be used as "firing archives" [4–6]. Along with this, iron oxide nanoparticles are considered a significant source of anthropogenic pollutants with potential effects on human health [7,8].

According to the classical concept of L. Néel [9], at a sufficiently small volume of a ferromagnetic particle or at elevated temperature, thermal fluctuations are able to overcome the energy barrier between states with opposite orientations of the magnetic moment. In this case, the momentum makes spontaneous reorientations, and the particle behaves as a superparamagnetic particle. The key parameter is the blocking volume v_b, which sets the boundary between the blocked and superparamagnetic states. The blocking volume is defined as $v_b = \frac{2k_BT}{I_s(T)H_0(T)}\ln(tf_0)$, where t is the measurement time; T is the temperature at which the measurements are carried out; I_s is the spontaneous magnetization; H_0 is the intrinsic magnetization reversal field (microcoercivity); k_B is the Boltzmann constant; and f_0 is the frequency factor.

For an ensemble of SP particles in a zero field, the average magnetization is zero, but an average moment directed along the field appears in an external field. The shape of the magnetization curves and the size of the blocking volume are significantly affected by interparticle interactions that change the distribution of relaxation times [9–11]. These effects lead to the appearance of magnetic viscosity and can contribute to the remanent magnetization.

The presence of superparamagnetic particles in soils and rocks can affect the results of geophysical surveys by the transient electromagnetic method (TEM soundings) [12]. It is known that transient processes distorted by the influence of superparamagnetism are characterized by the t^{-1} law, which is much slower than the decline of purely inductive response [13,14]. It has been shown that the use of electromagnetic sounding equipment in some cases allows detecting processes related to magnetic viscosity in field conditions [15–17], including archaeological studies [12,18,19]. Thus, the TEM method can be considered as one of the ways to study magnetic viscosity in the conditions of the natural occurrence of rocks.

In baked clays, magnetic properties are controlled by phase transformations of iron-bearing minerals during heating. As the temperature increases, hydroxides (e.g., goethite, lepidocrocite) dehydrate and transform into maghemite and magnetite, while further heating produces hematite or metastable phases such as ε-Fe_2O_3 [20,21]. These transformations control the balance between superparamagnetic and ferrimagnetic grains.

Of particular interest are polymorphic modifications of iron oxides formed by thermal action on clays. The most common phases—magnetite (Fe_3O_4), maghemite (γ-Fe_2O_3), and hematite (α-Fe_2O_3)—have different magnetic properties and thermal stability. At the same time, metastable modifications, such as ε-Fe_2O_3 and β-Fe_2O_3, are often formed by rapid heating and cooling and are characterized by unusual magnetic parameters, including high coercivity and pronounced superparamagnetic behavior [21]. Importantly, the ratio of these polymorphs depends on the temperature and cooling rate, making them reliable indicators of firing conditions [22]. The study of the set of iron oxide polymorphs in baked clays allows us to connect mineralogical transformations with the formation of various magnetic populations: from SP nanoparticles to larger ferrimagnetic grains. Thus, the nature of polymorphic transformations directly determines the proportion of SP particles and the evolution of magnetic properties during firing.

Despite considerable theoretical and experimental work, it remains rather unclear how the firing temperature regime affects the distribution of magnetic fractions: SP, ferri-, and ferromagnetic grains. The comparative evaluation between industrially baked bricks and laboratory baked samples, where the heat treatment conditions are controlled, is particularly underrepresented.

The present study uses a set of magnetic granulometry methods outlined in our previous works [23–27] that was extended to combine the use of magnetometry and TEM soundings, and to assimilate the experimental results into a theoretical framework modeling the magnetic state of the sample as a system of interacting single-domain particles. This approach allows us to estimate the particle size distribution of the magnetic fraction and, in particular, to calculate the content of SP ultrafine particles. We demonstrate the performance of our method by analyzing the magnetic properties of iron oxide nanoparticles found in baked clays (industrial bricks and laboratory brick samples). The magnetic parameters of these materials reflect both the mineralogical transformations occurring during firing and the specific conditions of thermal treatment. Their analysis provides insight into the mechanisms of mineral phase formation and enables reconstruction of the thermal history. By combining magnetic granulometry, Mössbauer spectroscopy, and low-temperature magnetometry, we quantify the contribution of superparamagnetic particles and reveal the microstructural magnetic heterogeneity of baked clays subjected to different firing regimes. This interdisciplinary approach allows us not only to evaluate the contribution of the SP fraction but also to reconstruct the microheterogeneity of the magnetic structure, reflecting the thermal history of the samples. This study uniquely combines TEM soundings with magnetometry and theoretical modeling of interacting particles.

It should be noted that in the present work, for the first time, an approach has been formulated in general form, previously applied to a wide range of objects [23–27], which allows for the qualitative and quantitative analysis of the magnetic characteristics and magnetic states of samples, including various ferrimagnetic fractions even at volume concentrations significantly less than one percent. A distinctive feature of this approach is the iterative process of agreement between experimental data and the results of calculations of the magnetizations of dilute magnets, taking into account the dipole–dipole interparticle interaction.

2. Materials and Methods

2.1. Materials

Clay from the Leningrad region (ClayL) served as the base material for two types of bricks: industrial (Ind) and laboratory (Lab). The industrial bricks were produced at the "ETALON" construction materials plant (Leningrad region, Russia). The firing process, from room temperature up to 995 °C and back, lasted three days. The Lab bricks with approximately 1 × 1 × 1 cm sides were initially formed manually using the same clay. Then they were slowly (during 15 h) heated in air up to 995 °C and cooled down for an additional 15 h in a furnace.

2.2. Experimental and Theoretical Methods

The microstructure and elemental composition of the samples were studied using scanning electron microscopes Hitachi TM-3000 (Hitachi, Tokyo, Japan) and Zeiss Merlin (Carl Zeiss, Oberkochen, Germany). Secondary (SE) and reflected electron (BSE) registration modes were used for analysis. The samples were prepared in the form of polished sections, the surface of which was covered with a ~10 nm thick carbon layer to prevent charging. The accelerating voltage was 15–20 kV, and the working distance was ~8 mm. Energy dispersive X-ray microanalysis was performed using an Oxford Instruments AZtec system,

version 2.1 (for Hitachi) and an integrated Si(Li) based detector (for Zeiss). Quantification was performed using the ZAF-correction method without the use of standards, and the accuracy of determination of major elements was 1–2 wt. %. Images were obtained at different magnifications (from 500× to 20,000×), which allowed for characterization of both the overall texture and morphology of individual iron oxide grains.

The phase composition of the samples was determined by powder X-ray diffraction on a Bruker D2 Phaser diffractometer (Bruker, Billerica, MA, USA) using CuKα radiation (λ = 1.5406 Å). The imaging was performed in the range of 2θ angles from 5° to 80° with a step of 0.02° and an accumulation time of 1 s per point; the samples were rotated during the measurements to reduce texture effects. Data processing was performed with the PDXL-2 software package (Rigaku, Tokyo, Japan) using the PDF-2 database (ICDD, version 2011). Quantitative phase analysis was performed using the Rietveld method [28]. The quality of approximation was evaluated by the Rwp and χ^2 criteria, which for all samples were within the limits typical of a correct phase analysis. The PDXL-2 refinement database (Rigaku, Japan) uses PDF-2 entries (ICDD 2011), which include the ε-Fe_2O_3 reference pattern (PDF#39-1346 for the orthorhombic form). This pattern was included in the Rietveld analysis alongside the main phases.

Mössbauer spectra of ^{57}Fe were recorded at room temperature in the pass-through geometry on an SM-2201 spectrometer (RF) with a ^{57}Co source of activity ~$1.5 \cdot 10^9$ Bq. The velocity scale was calibrated using a 6 μm thick α-Fe foil. The absorber thickness was 10–12 mg/cm^2, and the velocity range was ±4 mm/s. The spectra were approximated using the MossFit program (IGHD RAS). Models of doublets (γ-Fe_2O_3, Fe^{3+} in octahedral position) and sextets (Fe_3O_4, α-Fe_2O_3), as well as probability distributions of hyperfine magnetic fields for nanophases, were used in the processing. Isomeric shifts were given relative to α-Fe at 295 K.

Magnetic properties were measured using two instruments: (i) MPMS SQUID VSM (Quantum Design, San Diego, CA, USA): temperature range 1.8–1000 K; magnetic field up to 7 T; sensitivity ~10^{-11} A·m^2; (ii) Lake Shore 7410 VSM (Lake Shore Cryotronics, Westerville, OH, USA): temperature range 4.4–450 K; magnetic field up to 1.8 T; sensitivity ~10^{-8} A·m^2. Hysteresis loops and remanence demagnetization curves provided the saturation magnetization (M_s), remanent saturation magnetization (M_{rs}), coercivity (H_c), and remanent coercivity (H_{cr}). The temperature dependencies of the remanent magnetization were also measured in the range of 2–300 K using the following scheme: (i) measuring the LT-SIRM created in a 5 T field during heating with initial cooling in zero field, ZFC; (ii) measuring the LT-SIRM created in a 5 T field during heating with initial cooling in the presence of a field, FC; and (iii) measuring the SIRM created in a 5 T field in a cooling–heating cycle, RT-SIRM.

Anhysteretic remanent magnetization (ARM) and isothermal remanent magnetization (IRM) were measured on an SRM-755 cryogenic magnetometer (2G Enterprises, Lansing, NY, USA). Thermal demagnetization behavior was investigated following a three-axis Lowrie test [29]. An IRM was imparted to a cubic sample (1 cm^3) in three orthogonal directions at progressively lower fields (e.g., 1 T, 0.2 T, 0.04 T) to target high-, medium-, and low-coercivity phases. The sample was then heated stepwise (1 °C increments), measuring remanent magnetization to characterize distinct coercivity fractions.

AC magnetic susceptibility was measured using two complementary instruments: (i) an MFK1-FA kappa-bridge (AGICO, Brno, Czech Republic) operated at three discrete excitation frequencies (976, 3904, 15,616 Hz), at AC field amplitudes 5–700 A m^{-1}; (ii) a PPMS-9 (Quantum Design, USA) equipped with the ACMS II option, covering 11–10,000 Hz with an excitation amplitude of 26 A m^{-1} over 2–300 K.

The values of magnetic susceptibility obtained on two installations at 295 K with the following parameters were used for calculation: (1) MFK1-FA (AGICO, Brno, Czech Republic), f_l = 976 Hz, f_h = 15,616 Hz, amplitude of the alternating field 5 A/m for Ind and Lab samples and 50 A/m for ClayL; (2) PPMS-9 (Quantum Design, San Diego, CA, USA), f_l = 11 Hz, f_h = 10,000 Hz, amplitude of the field 26 A/m. We should also note the following. In our measurements, the MFK1-FA (kappa-bridge) records the total magnetic susceptibility χ, with no obvious separation into real χ' and imaginary χ'' components. In PPMS-9 with the ACMS II option, on the contrary, both χ' and χ'' are determined directly, i.e., real and imaginary components are clearly separated in the measurement system. In our case, χ'' is of order 10^{-7} and χ' is of order 10^{-4}–10^{-3}, the imaginary part being less than 0.1% of χ'. In such a case, the total χ measured on MFK1-FA is almost the same as χ' because $\chi'' << \chi'$. Moreover, the technical characteristics of the MFK1-FA (sensitivity up to $2 \cdot 10^{-8}$ SI) ensure that the imaginary component is below the existing threshold, so the χ measurements on the MFK1-FA correctly reflect the real component for our samples. This allows us to use both data sets to jointly analyze the frequency dispersion of susceptibility.

Measurements of pulse transient characteristics of magnetization of samples of baked clays were carried out on the laboratory setup described in [26]. For registration of transient characteristics, we used standard equipment for TEM sounding, the TEM-FAST instrument [30]. The laboratory setup is a custom-built two-coil coaxial system. The generator coil is connected to the output of the TEM-FAST instrument, and the receiver coil to the input of the instrument. The working volume of the measuring cell is 75 cm^3. The operating time range, limited at small times by the duration of the system's own transient process, and at large times by the noise level of the equipment (about 0.1 μV), for the studied samples was 25–1000 μs. The ratio of pulse duration to pause duration in TEM-FAST equipment is 3:1.

This work uses a modification of the method for calculating the distribution function of random dipole–dipole interaction fields in dilute magnets. The approach is based on the decomposition of the distribution function into a Gram–Charlier series using Bell polynomials, which greatly simplifies the calculation of the magnetization of an ensemble of magnetostatically interacting particles [31]. The model allows for the magnetization of the ensemble, the volume fractions of particles in different magnetic states, the concentration of ferrimagnetic material, and the effective values of spontaneous and remanent saturation magnetization to be estimated from experimental hysteresis characteristics. Unlike traditional computer micromagnetic modeling (see, for example, [32–34]), which often does not take into consideration chemical heterogeneity, variations in particle size and magnetic states, and also has limitations on the number of simulated elements, the proposed approach allows these difficulties to be circumvented for both natural and artificial objects [25,27,35].

By using the approximation of lognormal particle distribution by volume [36,37], the fractions of particles in different magnetic states can be calculated [25]. In modeling, the range of particles is divided into 5 intervals: superparamagnetic (SP and bSP), single-domain (SD), pseudo-single-domain (PSD), and multi-domain (MD). The range of superparamagnetic particles contains unblocked superparamagnetic ones (SP) that do not contribute to the remanent magnetization, as well as superparamagnetic particles blocked by magnetostatic interaction (bSP) that contribute not only to the saturation magnetization but also to the remanent magnetization (see, for example, [11]).

3. Experimental Results

3.1. Structure-Phase Composition: Results and Interpretation

SEM images (Figure 1) show the presence of iron oxides localized in pores and cracks of all studied samples. They are represented by small isometric grains and their aggregates, the size of which in some cases is 0.1–0.2 μm (Figure 1a–d).

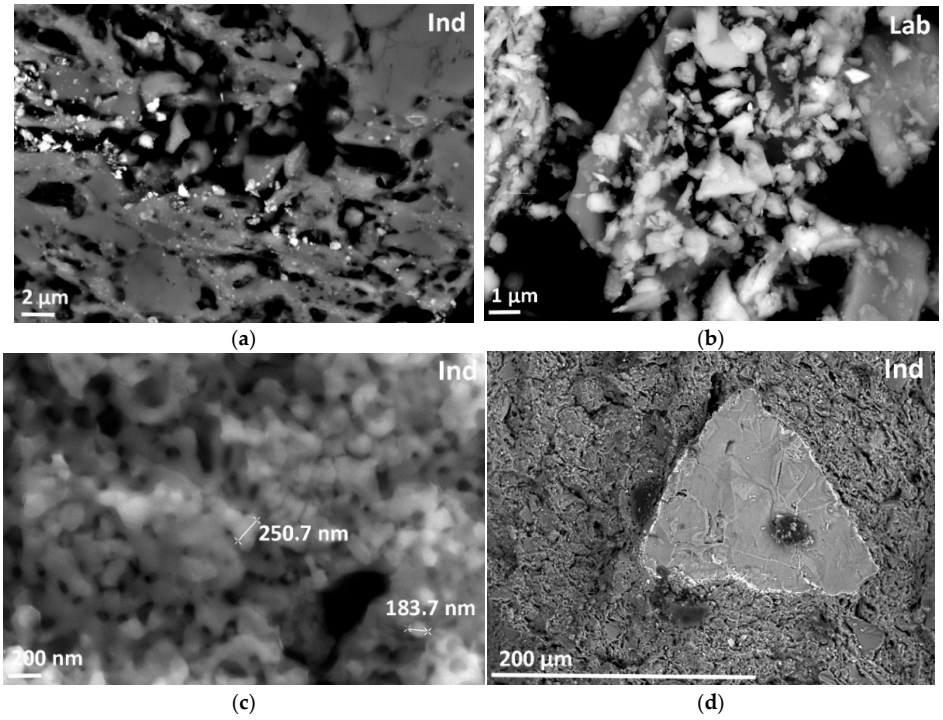


Figure 1. SEM images with grains and aggregates of a varying morphology: sample Ind, high (**a**,**c**) and low magnification (**d**); sample Lab (**b**).

The results of the quantitative phase analysis (Table 1) demonstrate that the thermal transformation of the initial clay (ClayL) is accompanied by the decomposition of kaolinite, chlorite, amphiboles, and carbonates with the subsequent formation of feldspars, hematite, and spinel phases. Up to 8% of spinel is found in the Ind sample, whereas in the Lab sample, this phase is absent. The convergence of the calculated and experimental profiles (Rp) is 4.4–5.9%, which confirms the correctness of the phase analysis.

Table 1. Quantitative phase analysis of the samples (wt. %) according to full profile analysis by the Rietveld method.

	ClayL	Ind	Lab
Quartz	40	44	49
Feldspar (microcline + plagioclase)	23	39	41
Mica	20	3	4
Amphibole	2	1	1
Hematite	—	5	5
Spinel	—	8	—
Kaolinite	9	—	—
Pyroxene	2	—	—
Chlorite	5	—	—
Dolomite	1	—	—
R_p (*) (%)	4.4	5.9	5.4

(*) $R_P = \frac{\Sigma\left|y_i^{obs} - y_i^{calc}\right|}{\Sigma y_i^{obs}}$ convergence factor of the calculated and experimental X-ray profiles, y_i-intensity at each experimental point of the X-ray image.

The Rietveld refinement indicated that ε-Fe_2O_3, if present, contributes <2 wt. % in total. Given the peak overlaps with hematite and spinel phases, and the inherent uncertainty in distinguishing orthorhombic and hexagonal iron oxides with similar lattice parameters at the resolution available, the presence of ε-Fe_2O_3 cannot be unambiguously confirmed from XRD data alone.

Further information on the degree of crystallization of iron oxide phases was obtained from the Mössbauer spectroscopy data.

3.2. Mössbauer Spectroscopy: Fe Valence and Magnetic Ordering

The Mössbauer spectra of the Lab and Ind samples at 300 K are approximated by a combination of four components: two paramagnetic doublets (Fe(1), Fe(2)) and two magnetically ordered sextets (Fe(3), Fe(4)) (Figure 2, Table 2). In both samples, the bulk of the spectrum belongs to high-spin Fe^{3+} ions, which are present both in paramagnetic (Fe(1)) form and as part of magnetically ordered phases (Fe(3), Fe(4)). The Fe^{2+} content is small (<2%). The total fraction of the magnetically ordered fraction (Fe(3) + Fe(4)) is ~49% for Lab and ~62% for Ind.

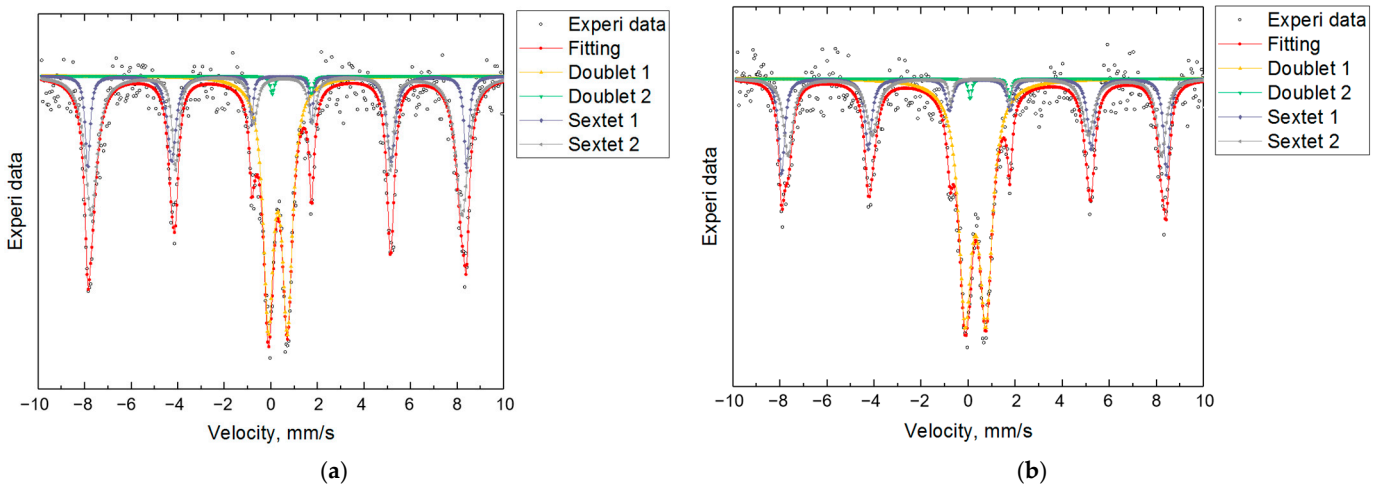


Figure 2. Mössbauer spectra of Ind (**a**) and Lab (**b**) samples.

Table 2. Parameters of Mössbauer spectra.

Sample	Component	Fe	IS (mm/s)	QS (mm/s)	B_{Hf} (T)	%
Lab	Doublet Fe(1)	Fe^{3+}	0.305 ± 0.009	0.882 ± 0.016	—	50.11
	Doublet Fe(2)	Fe^{2+}	0.910 ± 0.044	1.663 ± 0.089	—	1.29
	Sextet Fe(3)	Fe^{3+}	0.363 ± 0.012	0.241 ± 0.023	50.796 ± 0.097	22.82
	Sextet Fe(4)	Fe^{3+}	0.388 ± 0.017	0.228 ± 0.034	49.285 ± 0.205	25.78
Ind	Doublet Fe(1)	Fe^{3+}	0.293 ± 0.007	0.819 ± 0.012	—	36.92
	Doublet Fe(2)	Fe^{2+}	0.895 ± 0.057	1.675 ± 0.115	—	1.13
	Sextet Fe(3)	Fe^{3+}	0.353 ± 0.010	0.183 ± 0.021	50.543 ± 0.085	20.84
	Sextet Fe(4)	Fe^{3+}	0.372 ± 0.010	0.274 ± 0.021	49.496 ± 0.132	41.11

The difference in the content of ordered phases indicates a greater degree of crystallization of iron oxides in industrial bricks. Fitting quality parameters: Spectra were fitted to convergence with $\chi^2 < 1.5$ and residual uncertainties <1%. Constraints on IS, QS, and B_{hf} were based on the literature values for iron oxides. The Fe(1) doublet, present in both samples, reflects either residual paramagnetic Fe^{3+} or ultrafine SP particles.

3.3. Field Dependencies of Magnetization

Figure 3 shows examples of hysteresis loops and DC backfield curves, from which coercivity of remanence (H_{cr}) is determined.

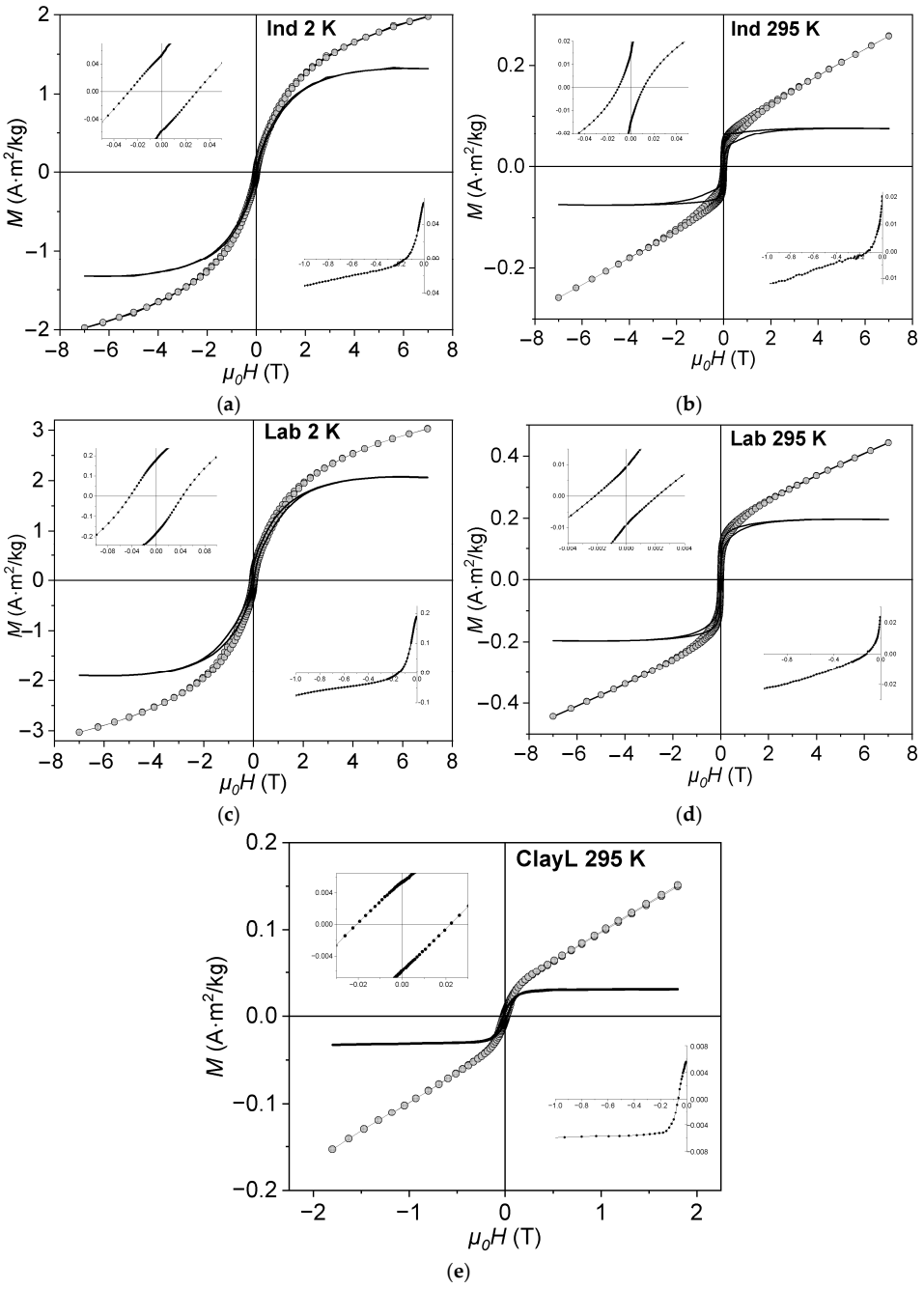


Figure 3. Hysteresis loops and determination of coercivity from remanent magnetization of the samples Ind at 2 K (**a**) and 295 K (**b**), Lab at 2 K (**c**) and at 295 K (**d**), and ClayL at 295 K (**e**). The gray curve corresponds to the original data, and the black curve takes into account the correction for the paramagnetic component. On insets: central parts of loops and remanent magnetization destruction curves.

Table 3 summarizes the characteristics of hysteresis loops and backfield curves.

At 2 K, both Ind and Lab samples show significantly higher values of saturation magnetization (up to 2.0 A·m^2/kg for Lab and 1.3 A·m^2/kg for Ind) and remanent magnetization compared to the original unfired clay (ClayL). Under the same conditions, high values of

coercivity and coercivity of remanence are recorded. For both fired samples, a ~2–4 mT displacement of the loops relative to the zero field is observed (see insets in Figure 3).

At 295 K, the loops become narrower and more symmetric. The values of M_s and M_{rs} decrease, and the H_{cr}/H_c ratio changes, reaching 59.5 for Lab.

Table 3. Hysteresis characteristics of the samples. In parentheses in the Samples column, the measurement setup and the hysteresis measurement temperature in K are indicated.

Sample	M_s, A·m²/kg	M_{rs}, A·m²/kg	M_{rs}/M_s	$\mu_0 H_c$, mT	$\mu_0 H_{cr}$, mT	H_{cr}/H_c
ClayL (Lake Shore 295)	0.03	0.005	0.17	17	64	3.8
Ind (MPMS 2)	1.30	0.060	0.05	28	150	5.4
Ind (MPMS 295)	0.08	0.020	0.25	10	139	13.9
Lab (MPMS 2)	2.00	0.190	0.10	45	150	3.3
Lab (MPMS 295)	0.20	0.020	0.10	2	119	59.5

3.4. Coercivity Spectra and Remanent Magnetization

Demagnetization of ARM in an alternating field allowed us to construct ARM demagnetization curves and the corresponding coercivity spectra (Figure 4). In the Ind sample, the spectrum is broad, with a maximum in the range of 10–40 mT and an extended "tail" at values above 40 mT. In the Lab sample, the spectrum is narrower, with a maximum around 10 mT.

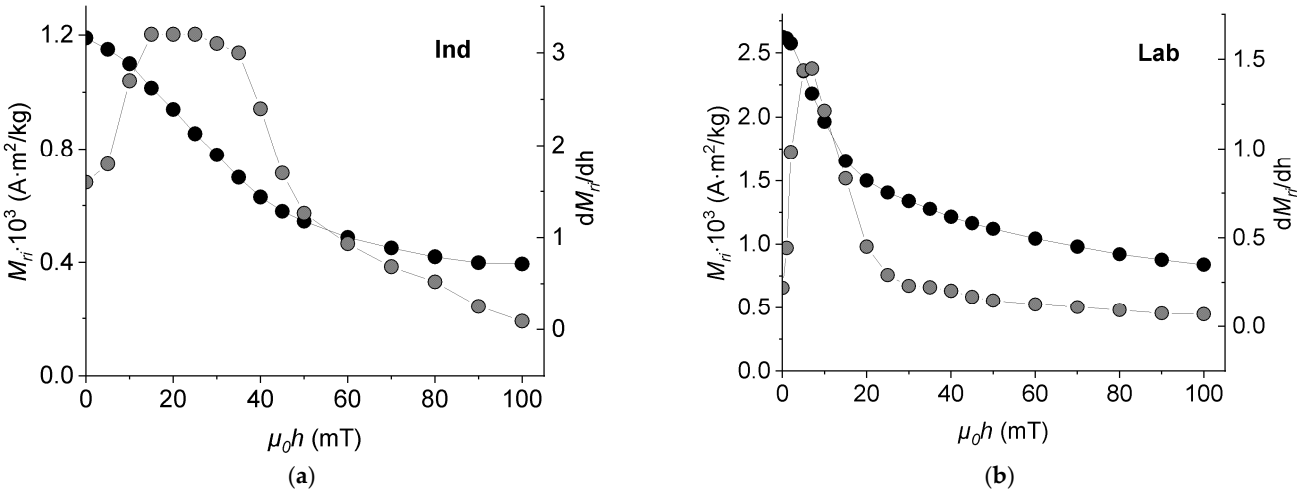


Figure 4. ARM destruction (black) and its coercivity spectrum (gray) for samples Ind (**a**) and Lab (**b**). The ARM was created in a constant field of 0.5 mT, and the destruction was carried out in an alternating field *h*.

Figure 5 shows the thermal demagnetization curves of the three components of the saturated remanent magnetization (IRM) magnetized in 0.04 T, 0.2 T, and 1 T fields for the Ind sample (Lowry method). Each curve characterizes fractions with different coercivity: low, medium, and high, respectively.

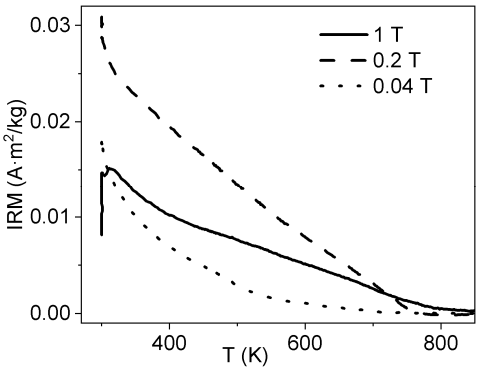


Figure 5. Thermal demagnetization of 3-component IRM for Ind sample.

The component with a coercivity of 0.2 T shows a sharp decrease in magnetization starting from ~320 K and complete demagnetization at ~750 K. The component with a coercivity of 0.04 T has a relatively high initial value (~0.017 A·m^2/kg) and gradually loses magnetization up to ~790 K. The component with coercivity of 1 T is characterized by a low initial magnetization (~0.008 A·m^2/kg), which increases upon heating up to ~320 K and then decreases smoothly with complete demagnetization at ~870 K.

3.5. Low-Temperature Magnetization

Figure 6 shows the temperature dependencies of the remanent magnetization measured using two protocols: LT-SIRM (after field cooling, FC, and zero field cooling, ZFC; gray and black colors, left axis) and RT-SIRM (after magnetization at room temperature; blue curve, right axis).

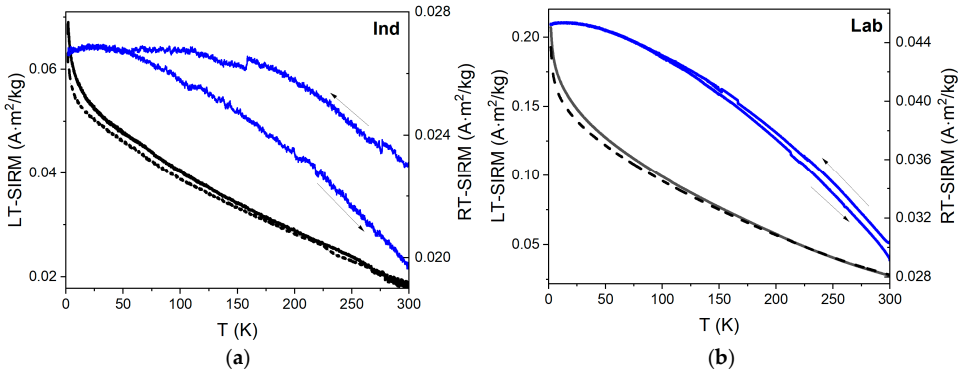


Figure 6. Low-temperature magnetization measurements for Ind (**a**) and Lab (**b**) samples. LT-SIRM: gray FC, black ZFC; RT-SIRM blue curve.

For the Ind sample, the LT-SIRM values at 2 K are ~0.07 A·m^2/kg. The curves diverge at low temperatures and maintain the difference up to 300 K. The RT-SIRM curve shows a discrepancy between the cooling and heating courses; at 2 K, the value is 0.0197 A·m^2/kg compared to the initial 0.023 A·m^2/kg, corresponding to a decrease of about 15%. In the Lab sample, the LT-SIRM value at 300 K is much higher and reaches ~0.2 A·m^2/kg. The difference between the FC and ZFC curves is observed only at low temperatures and decreases with increasing temperature, practically disappearing by 150–200 K. The RT-SIRM of this sample has a value of about 0.045 A·m^2/kg at 2 K and decreases to ~0.03 A·m^2/kg at 300 K, which corresponds to a loss of about 3%.

3.6. Impulse and Frequency Characteristics of Susceptibility

3.6.1. Impulse Characteristics

The impulse transient responses of the industrial (Ind) and laboratory (Lab) brick samples, each averaged over five realizations, are presented in Figure 7. The useful signal exceeds the noise level of the receiving channel by more than an order of magnitude. In the time range of 25–1000 μs, the decay of the signal is well approximated by a power-law dependence: $\varepsilon(t)/I_0 = a \cdot t^{-b}$, where the exponent b significantly exceeds 1. This indicates the presence of a superparamagnetic component and reflects a broad, non-uniform distribution of relaxation times [23]. At the same time, the values of b are similar for both samples.

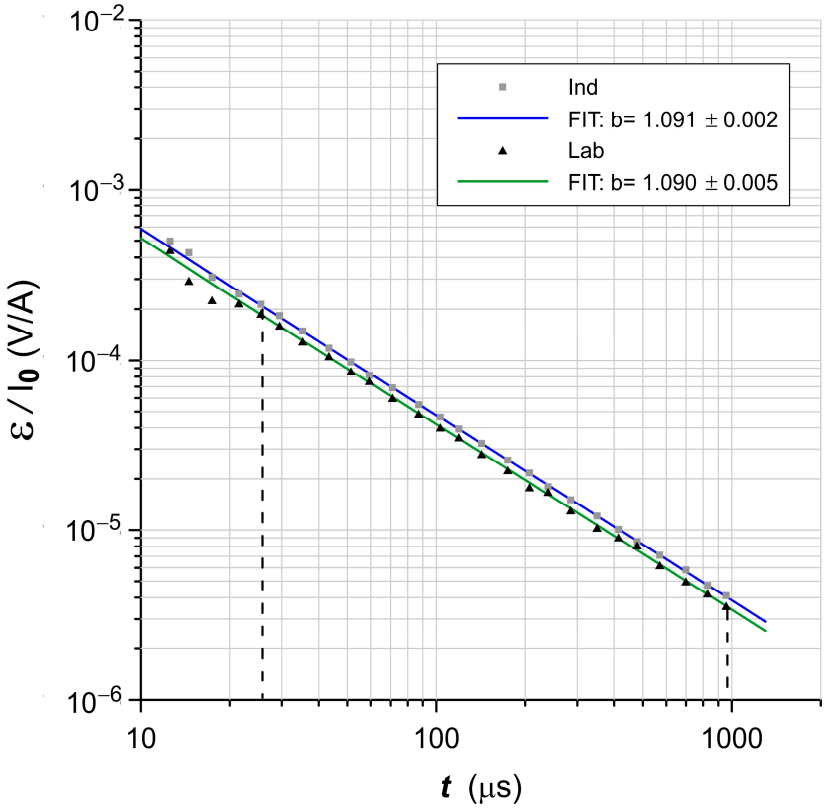


Figure 7. Impulse transient characteristics of industrial (gray dots) and laboratory (black dots) brick samples and their power-law approximations in the time interval 25–1000 μs (blue and green lines, respectively). The error estimates for the exponent b correspond to standard deviations.

3.6.2. Frequency–Temperature and Frequency–Field Dependencies of Magnetic Susceptibility

Figure 8 shows the temperature dependencies of the magnetic susceptibility χ' measured at different frequencies for the Ind and Lab samples. In the Ind sample, χ' shows a distinct minimum in the region of 20–30 K, followed by a smooth increase up to 300 K. At 2 K, the susceptibility values of ~$1.2 \cdot 10^{-3}$ m^3/kg are observed, which then drop rapidly to form a temperature minimum. With increasing frequency, the curves gradually shift downward, and the position of the minimum χ' is also observed to shift toward higher temperatures as the frequency increases, which is characteristic of the temperature-dependent relaxation of magnetic moments. In the Lab sample, χ' is much higher in absolute value of ~$5 \cdot 10^{-3}$ m^3/kg at 300 K and shows a smooth growth from 2 to 300 K. The curves, as in the Ind case, diverge as a function of frequency: at higher frequencies, the values of χ' are lower, and frequency dispersion is observed. The temperature minimum is near 10–15 K and is smoothed.

Thus, both samples exhibit a frequency–temperature dependence of χ', but the behavior differs in both amplitude and shape of the curves.

All three samples were tested for the frequency–field dependence of magnetic susceptibility (Figure 9).

In unbaked clay, χ depends weakly on frequency and magnetic field amplitude, remaining at a low level over the entire range. The annealed samples show a pronounced frequency dependence over the entire range of the alternating magnetic field.

Thus, the obtained dependencies $\chi(f, T)$ and $\chi(f, h)$ confirm the presence of significant differences in magnetic susceptibility between samples, reflecting inhomogeneities in the composition and distribution of magnetic states. A quantitative evaluation of these differences is given in the next subsection using the FD factor.

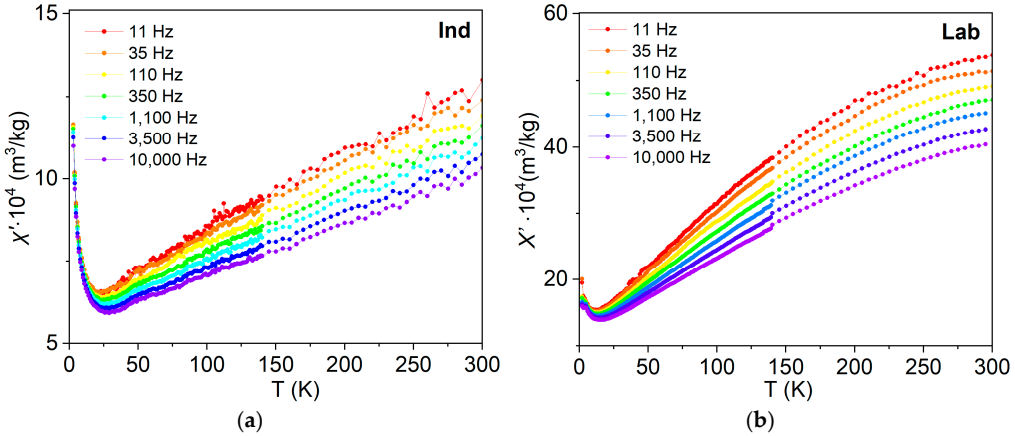


Figure 8. Frequency–temperature dependencies of magnetic susceptibility of Ind (**a**) and Lab (**b**)samples.

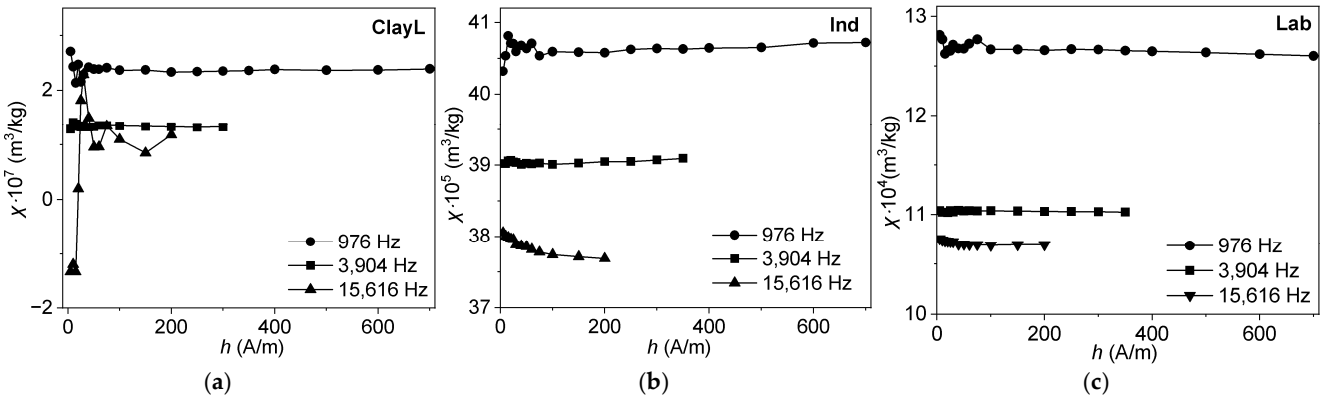


Figure 9. Frequency–field dependencies of magnetic susceptibility of ClayL (**a**), Ind (**b**), and Lab (**c**) samples.

3.7. FD Factor and SP Contributions

To evaluate the contribution of superparamagnetic particles to the magnetic susceptibility of the studied samples, a modified FD factor calculated according to the methodology was used [38]. The value of the FD factor is determined by the following formula:

$$fd = \frac{\chi_{f_l} - \chi_{f_h}}{\chi_{f_l} \log\left(\frac{f_h}{f_l}\right)} \cdot 100\%, \quad (1)$$

where χ_{f_l} and χ_{f_h} are susceptibilities at the low f_l and high f_h frequencies, respectively.

These calculations are summarized in Table 4.

Table 4. FD factor values at room temperature.

Sample	*fd*, %		
	MFK1-FA	**PPMS-9**	**Average Value**
Ind	5.2	7.8	6.5
Lab	12.5	8.5	10.5
ClayL	50 (estimation)	–	–

The combination of structural, spectroscopic, and magnetic measurements reveals systematic differences in mineral transformations, magnetic phase composition, and domain state distributions between the industrially and laboratory baked samples. These differences reflect the influence of baking conditions on the formation and evolution of superparamagnetic and ferrimagnetic components.

4. Discussion of the Experimental Results

4.1. Structure-Phase Basis of Magnetic Microheterogeneity

Microstructural and phase characteristics of the investigated samples of fired clay confirm the formation of their magnetic properties under conditions of a microheterogeneous system and allow us to interpret some features of their magnetic properties caused by thermal treatment.

Scanning electron microscopy (Figure 1) shows that iron-bearing phases are represented by isometric grains and their aggregates < 0.2 μm in size, localized in pores, cracks, and along the boundaries of relict minerals. Such arrangement and dispersity indicate their secondary origin associated with dehydration of iron hydroxides (goethite, lepidocrocite) at late stages of firing and during cooling [39].

X-ray phase analysis (Table 1) showed the destruction of the original clay minerals (kaolinite, chlorite), amphiboles, and carbonates with the formation of feldspars, hematite, and spinel phases. Spinel was detected only in the commercially fired Ind sample in an amount of up to 8 wt. %, reflecting more intensive thermal exposure ($T \geq 950$ °C, prolonged exposure) and consistent with the literature data on high-temperature stabilization of spinels [40–42].

Mössbauer spectroscopy further clarifies the valence and structural state of iron, revealing four components: two paramagnetic doublets and two magnetically ordered sextets (Table 2, Figure 2). The total fraction of magnetically ordered Fe^{3+} (Fe(3) + Fe(4)) is higher in Ind (~62%) compared to Lab (~49%), confirming a more pronounced development of magnetic phases during industrial roasting [43,44]. At that, the Fe(1) doublet, characteristic of high-spin Fe^{3+} in amorphous or disordered media, remains the main component [6,45,46]. Its presence in both samples can be associated with both residual iron in the aluminosilicate matrix and ultradisperse SP particles in a state of dynamic disorder at room temperature. Although the Mössbauer data at 300 K are not sufficient to unambiguously distinguish paramagnetic and superparamagnetic states, the presence of this component supports the hypothesis of magnetic microheterogeneity [47].

Magnetically ordered Fe(3) and Fe(4) sextets (IS ≈ 0.35–0.39 mm/s; B_{Hf} ≈ 49–51 T) are characteristic of Fe^{3+} in ferrimagnetic or antiferromagnetic oxides—hematite, maghemite, or defective forms of magnetite [2]. Relatively low values of quadrupole splitting (QS ≈ 0.18–0.28 mm/s) testify to the symmetric environment of iron ions and a high degree of crystallinity of these phases. The presence of a highly coercive fraction similar to ε-Fe_2O_3 previously found in fired clays cannot be excluded [42,44,48,49].

Phase differences between the samples determine the balance of superparamagnetic and ferrimagnetic components: in Ind, more intensive firing leads to an increase in ordered

spinel phases and a decrease in the proportion of SP grains, whereas in Lab, a greater contribution of amorphous and finely dispersed iron is retained [50]. The totality of the data discussed in this section provides direct evidence for the coexistence of several iron-bearing phases in the annealed samples. These structural-phase differences provide a basis for analyzing the results of magnetic measurements and applying the theoretical model developed by the authors.

4.2. Magnetic Parameters as Indicators of a Multicomponent Ensemble of Particles

The hysteresis parameters (Table 3) reflect the multicomponent nature of the magnetic system and allow us to evaluate the contribution of different fractions. At 2 K, the Lab sample shows the highest saturation magnetization $M_s \approx 2.0$ A·m^2/kg and appreciable remanent magnetization, whereas Ind is characterized by a lower value of $M_s \approx 1.3$ A·m^2/kg but higher coercivity H_c = 28 mT, H_{cr} = 150 mT. The 2–4 mT shift of the hysteresis loop observed at 2 K for both samples is relatively small: for the classical exchange bias effect, values typically exceed 10 mT [51]. Nevertheless, its presence may indicate interface exchange interactions in core–shell structures (e.g., magnetite/maghemite/hematite) [52,53] or in systems containing ε-Fe_2O_3, which are known for their anomalous coercivity and possible contribution to exchange bias [54]. At 295 K, the loops of both samples narrow (the "wasp waist" effect), which is due to thermal unlocking of the magnetic moments of superparamagnetic particles, and there is no exchange bias effect [55,56].

The unusually high $H_{cr}/H_c \approx 60$ in the Lab sample at 295 K attracts attention. Such high values can be related not only to the presence of SP particles but also to a sufficiently strong magnetostatic interaction in the ensemble of fine particles, which enhances the difference between the reversible and irreversible components of magnetization. Thus, the H_{cr}/H_c parameter can be interpreted as an indicator of a high concentration of superparamagnetic and small ferrimagnetic grains in the ensemble [54,57–59]. Magnetostatic interactions between particles, especially in ensembles with a high concentration of magnetic grains, can significantly affect the coercivity characteristics [60].

The M_{rs}/M_s and H_{cr}/H_c ratios vary in a wide range, which is consistent with the hypothesis of a multicomponent ensemble, which is a mixture of low- and high-coercivity and SP particles. The small values of M_{rs}/M_s at anomalously high H_{cr}/H_c confirm that the magnetic properties are formed under conditions of strong particle interaction and wide dispersion in size and blocking temperatures [56,57]. Thus, the hysteresis parameters reflect the multicomponent nature of the ensemble of ferrimagnetic particles [54,59,61].

4.3. Temperature Dependencies of ARM and IRM Coercivity

The coercivity spectra obtained during ARM demagnetization show significant differences between the samples (Figure 4). In the Lab sample, the spectrum is narrow, with a maximum around 10 mT, indicating the predominance of soft ferrimagnetic fractions interpreted as maghemite or finely dispersed non-stoichiometric magnetite [62]. The spectrum of the Ind sample is broader, with a maximum in the 25 mT region and an extended "tail" in the > 40 mT zone. This tail may be due to the presence of highly coercive phases, including ε-Fe_2O_3, which has T_c~500 K and an anomalously high coercivity [21,42].

The results of the three-component Lauri test for IRM in the fields of 0.04, 0.2, and 1 T provide additional information on the temperature stability of the fractions (Figure 5). The main contribution to the magnetization of the Ind sample is made by the fraction with coercivity < 0.2 T, the magnetization of which starts to decay already at 320 K and disappears at 750 K. This behavior indicates the predominance of pseudo-single-domain particles of maghemite or non-stoichiometric magnetite [62,63]. The fraction with coercivity < 0.04 T

demagnetizes more smoothly and completely loses magnetization at 790 K, which is consistent with the presence of the magnetically soft fraction [61,64].

The high-coercivity fraction > 1 T shows an atypical behavior. Its magnetization increases upon heating up to 320 K, which may be related to the thermally stimulated unblocking of superparamagnetic particles or a phase transition within oxide nanophases. Then, there is a smooth decrease in magnetization with complete disappearance of IRM at 870 K, which probably corresponds to hematite [21].

Thus, the concordant ARM thermal fracture data and the three-component Lauri test confirm the presence of low-coercivity ferrimagnetic particles (maghemite/magnetite) and high-coercivity particles (hematite, ε-Fe_2O_3) in the samples [42,48]. The joint existence of these fractions forms a complex ensemble with overlapping distributions of coercivity and blocking temperatures, which is an important manifestation of magnetic microheterogeneity of fired clays.

4.4. Low-Temperature Magnetic Behavior

Low-temperature magnetic measurements characterize the thermostability of the remanent magnetization and the degree of magnetic reversibility of the samples, reflecting the variety of blocking temperatures and relaxation characteristics. The LT-SIRM and RT-SIRM curves obtained by different cooling protocols show different behavior of the Ind and Lab samples (Figure 6). In the Ind sample, the LT-SIRM values of about 0.07 A·m^2/kg are recorded at 2 K. A noticeable cleavage between the FC and ZFC curves is observed, which persists up to 300 K. This indicates the presence of a fraction with a high blocking temperature that irreversibly fixes the remanent magnetization depending on the cooling regime [65,66]. The RT-SIRM curve also exhibits significant thermomagnetic irreversibility: upon cooling, the magnetic moment drops by ~20% relative to the value at 300 K, and the cooling curve does not coincide with the heating curve. This behavior is characteristic of fractions with unstable magnetic configuration subject to rearrangement with temperature change [67,68]. The curves of sample Ind lack an explicit Verwey transition (~120 K for magnetite), which may indicate partial maghemitization of magnetite or fine dispersion of iron oxide phases [68].

In the Lab sample, the LT-SIRM values at 2 K are much higher (> 0.2 A·m^2/kg), but the splitting between the FC and ZFC curves is pronounced only at low temperatures and disappears above ~150–200 K. This indicates a narrower range of blocking temperatures and the predominance of fractions with lower stability of remanent magnetization [65,66]. The RT-SIRM curve shows high reproducibility under cooling and heating: the total magnetic moment loss is only ~3%, indicating a significantly lower thermomagnetic irreversibility compared to Ind [67].

This difference in thermostability is consistent with the results of the coercivity and FD factor analyses: Lab is dominated by softer ferrimagnetic and SP components that unlock at T > 150 K, while Ind contains stiffer components that are resistant to temperature fluctuations [55,61]. The behavior of the RT-SIRM and the ZFC and FC curves is also consistent with the distribution over the relaxation times revealed in the pulse measurements.

4.5. Frequency-Dependent and Transient Susceptibility Signatures of SP Particles

The studied samples clearly contain superparamagnetic particles that influence magnetic properties. Their presence is confirmed by the frequency dependence of magnetic susceptibility, impulse responses, and a rather large value of the FD factor. The FD factor calculated from the magnetic susceptibility data at different frequencies (Table 4) allows us to estimate the contribution of the superparamagnetic component. The Ind sample shows a moderate FD factor, 6.5% on average. This sample is probably dominated by larger grains

with blocked magnetic moments that do not have time to relax in this frequency range. The Lab sample shows a significantly higher FD factor, 10.5%, especially as measured by MFK1-FA (12.5%), indicating the presence of a larger quantity of SP particles [6]. ClayL (initial clay) shows the largest effect. But the FD factor in this case is most likely overestimated because it was evaluated in a large field (50 A/m) due to the instability of the magnetic susceptibility of the sample in fields below this value. However, the presence of SP particles is characteristic of clay materials [6], but this sample is not discussed further.

The temperature dependence of the magnetic susceptibility χ'(T) (Figure 8) also indicates the presence of relaxing magnetic moments. In the Ind sample, χ' shows a pronounced minimum in the region of 20–30 K, the position of which shifts with the change in frequency, which is a characteristic sign of the temperature relaxation of SP states. The Lab sample exhibits smoother behavior but also records a frequency dispersion χ'. These observations confirm the presence of an ensemble of particles with distributed relaxation times [38,69]. The frequency dispersion χ' and its temperature dependence emphasize the heterogeneity of the ensemble of ferrimagnetic particles in fired clays [59].

The impulse response measured for the Ind sample by the TEM method shows signal attenuation according to the step law with the exponent of degree ≥ -1 (Figure 7). This behavior indicates a broad and non-uniform distribution of the relaxation times of magnetic moments [13]. Such characteristics have been previously observed in natural and synthetic systems containing SP components and are related to the polydispersity of particles, heterogeneity of their shape and chemical composition, and interparticle interactions [25,27].

The paramagnetic "tail" of the Curie magnetic susceptibility observed at temperatures below ~20 K, especially in the Ind sample, provides additional evidence for the presence of SP particles. The growth of χ' with decreasing temperature is described by the law χ'~1/T and may be due to unpaired surface spins, isolated Fe^{3+}-centers, or frustrated states in clusters of nanoparticles [70–72].

Thus, the joint analysis of the FD factor, $\chi(f, T)$, impulse characteristics, and temperature behavior of the susceptibility indicates the presence of blocked and true SP particles in the samples, which determine the relaxation properties of the samples, especially in the region of low temperatures and weak fields.

5. Theoretical Modeling

The saturation magnetization of all samples (Table 3) is rather small. Assuming that the weak ferromagnet (hematite) is the main one, this does not correspond to the insignificant amount of hematite contained in the samples (Table 1). Consequently, the samples contain the ferrimagnetic fraction with concentrations of the order of per cent or less. This is confirmed by the results of Mössbauer spectroscopy (Table 2), showing the possible presence of maghemite. According to the Lauri test (Figure 5), the appearance of IRM fracture curves suggests the presence of at least two ferrimagnetic fractions. This is partially confirmed by the coercivity spectra of ARM (Figure 4), according to which the main contribution to the magnetization is made by ferrimagnet with coercivity of the order of 10–40 mT, but there is a rather noticeable highly coercive fraction, in which particles with coercivity higher than 100 mT are present, which is also evident from the high values of H_{cr} (Table 3). FC and ZFC measurements (Figure 6) also confirm that the spectrum for the Ind sample is broader and for the Lab sample it is narrower.

Thus, on the basis of magnetic and mineralogical data, two ferrimagnetic fractions with significantly different coercivity are assumed to exist in the studied samples. The first, less coercive fraction is assumed to consist of finely dispersed particles of maghemite and/or non-stoichiometric magnetite [25], the second, highly coercive fraction is assumed to be similar to ε-Fe_2O_3 [24,44,73,74].

Let us introduce the notion of the fraction of particles Δ_i constituting the i-th fraction. Fraction of particles n_{ik} of the first and second fractions in the corresponding five magnetic states (k = [1, 5], where 1 is the SP, 2 is the bSP, 3 is the SD, 4 is the PSD, and 5 is the MD):

$$n_{ik} = \Delta_i \int_{\alpha_{ik}}^{\beta_{ik}} \varphi(x)dx, \ \sum_i \sum_k n_{ik} = 1, \ \Delta_1 + \Delta_2 = 1, \tag{2}$$

where α_{ik} and β_{ik} are minimum and maximum volumes limiting the range of the k-th magnetic state for the i-th fraction. The probability density of the lognormal distribution is written as follows:

$$\varphi(x) = \frac{1}{x\sigma\sqrt{2\pi}} \exp\left(-\frac{(\ln(x/\mu))^2}{2\sigma^2}\right), \tag{3}$$

where $x = v/v_m$ is the particle volume reduced to the characteristic (mean) volume, σ is the standard deviation, and μ is the mathematical expectation of the corresponding Gaussian distribution.

Average volume and average particle size in the k-th state for the i-th fraction:

$$v_{ik} = \frac{\Delta_i}{n_{ik}} \int_{\alpha_{ik}}^{\beta_{ik}} x\varphi(x)dx, \ d_{ik} = (6v_{ik}/\pi)^{1/3}. \tag{4}$$

Then the average volume and average particle size of the whole ensemble are equal:

$$v_m = \sum_i \sum_k v_{ik} n_{ik}, \ d_m = (6v_m/\pi)^{1/3}. \tag{5}$$

Consequently, it is possible to express the volume concentrations of both fractions in different magnetic states:

$$c_{ik} = n_{ik}\frac{v_{ik}}{v_m}, \ \sum_i \sum_k c_{ik} = \sum_k c_{1k} + \sum_k c_{2k} = \Delta_1 + \Delta_2 = 1. \tag{6}$$

Particles consisting of ε-iron oxide are known to change to hematite when the size exceeds the order of 30 nm [74]. Therefore, the MD particles of the second fraction with a volume concentration of c_{25} can be distinguished as the third weakly magnetic fraction represented by hematite particles in the state close to SD. If we set the spontaneous magnetizations of these three fractions I_{si}, we can introduce the averaged spontaneous magnetization of the ferrimagnetic material in the sample:

$$I_s = I_{s1}\Delta_1 + I_{s2}(\Delta_2 - c_{25}) + I_{s3}c_{25}. \tag{7}$$

Then the volume concentration of ferrimagnetic in a sample of mass m and volume V can be estimated by the following formula:

$$c_f = \frac{M_s m}{I_s V}. \tag{8}$$

It should be further noted that in this work, due to the peculiarities of matching the experimental and theoretical hysteresis characteristics, magnetizations with different SI units are used:

(i) Experimental mass magnetizations M_s and M_{rs} (A·m^2/kg);

(ii) Theoretical volume magnetizations I_s, $I_{s\,eff}$, $I_{rs\,eff}$ (A/m), magnetization in the external magnetic field J (A/m), and dimensionless magnetization ζ.

The model of magnetostatically interacting single-domain particles with effective spontaneous magnetization (SDEM model) allows us to calculate values of $I_{s\ eff}$ and $I_{rs\ eff}$, consistent with experimental hysteresis characteristics (see, e.g., [25]). The modification of the SDEM model was used for calculating the distribution function of random fields of dipole–dipole interaction and effective spontaneous magnetizations in dilute magnetics using the expansion in the Gram–Charlier series with the help of Bell polynomials [31].

The magnetization ζ of an ensemble of interacting SD particles can be calculated using the following formula:

$$\zeta(H) = \frac{J}{c_f I_{s\ eff}} = 1 - 2\sum_{n=0}^{\infty} A_n \cdot Z_n(x_0), \tag{9}$$

where J is the magnetization in the external magnetic (Zeeman) field H and $I_{s\ eff}$ is an effective spontaneous (saturation) magnetization, taking into consideration the inhomogeneity of the ferrimagnetic material (the presence of different phases, fractions, domain structure, etc.). The coefficient A_n, depending only on the moments of the distribution function $W(H_i)$ over the interaction fields H_i, is equal to the following:

$$A_n = \frac{B_n(0, 0, k_3, k_4, ..., k_n)}{n!}, \tag{10}$$

where B_n are complete Bell polynomials, k_n is the n-th order cumulant. Function $Z(x_0)$ is calculated analytically and takes the following values:

$$Z_n(x_0) = \begin{cases} \frac{1}{2} - \frac{1}{2}\mathrm{erf}\left(\frac{x_0}{\sqrt{2}}\right), n = 0 \\ (-1)^n \varphi_u(x_0) \cdot He_{n-1}(x_0), n \geq 1 \end{cases}. \tag{11}$$

Here, $\mathrm{erf}\left(x_0/\sqrt{2}\right)$ is the error function, $\varphi_u(x_0)$ is the Gauss distribution, $He_n(x_0)$ is the Hermite polynomial, $x_0 = (H_0 + H + < H_i >)/\sigma$; $< H_i >$ and σ^2 is the mathematical expectation and variance of the distribution function $W(H_i)$, H is the external magnetic (Zeeman) field, and $H_0 \approx H_{cr}$ is the magnetization reversal field of the particles.

In this work, effective spontaneous magnetizations corresponding to experimental hysteresis characteristics are calculated. If $J = M_s\ m/V = c_f I_{s\ eff}$, then $\zeta = 1$. If $J = M_{rs}\ m/V = c_r I_{rs\ eff}$, then $\zeta = M_{rs}/M_s$, and c_r is the volume concentration and $I_{rs\ eff}$ is the effective spontaneous magnetization, taking into consideration the contribution of only bSP, SD, and PSD particles to the remanent magnetization. In this case,

$$c_r = c_f(1 - c_{11} - c_{15} - c_{21}). \tag{12}$$

Solving the inverse problem of finding $I_{s\ eff}$ and $I_{rs\ eff}$ by substituting the experimental values of saturation magnetization and saturation remanence requires additional data and assumptions.

Based on the experimental data, the effective spontaneous magnetizations of the three fractions are chosen so that $I_{s\ eff} = I_s$. Then the saturation magnetizations of the individual fractions are equal:

$$M_{s1} = M_s \cdot I_{s1}\Delta_1/I_s,\ M_{s2} = M_s \cdot I_{s2}(\Delta_2 - c_{25})/I_s,$$

$$M_{s3} = M_s \cdot I_{s3}c_{25}/I_s,\ M_{s1} + M_{s2} + M_{s3} = M_s. \tag{13}$$

The estimation of $I_{rs1\,eff}$ can be performed considering the magnetic states of the particles of the second and third fractions, i.e., by matching the values of $I_{rs2\,eff}$ and $I_{rs3\,eff}$, considering the experimental data:

$$I_{rs1\,eff} = \left[I_{rs\,eff} - I_{rs2\,eff}(\Delta_2 - c_{25}) - I_{rs3\,eff}c_{25}\right]/\Delta_1. \quad (14)$$

This allows us to estimate the contribution of the three fractions to the remanent saturation magnetization of the sample:

$$M_{rs1} = (c_{12} + c_{13} + c_{14})\frac{I_{rs1\,eff}}{I_{s1}}M_{s1},\ M_{rs2} = \frac{(c_{22} + c_{23} + c_{24})I_{rs2\,eff}}{(1 - c_{25})I_{s2}}M_{s2},$$

$$M_{rs3} = \frac{I_{rs3\,eff}}{I_{s3}}M_{s3},\ M_{rs\,est} = M_{rs1} + M_{rs2} + M_{rs3} \approx M_{rs}. \quad (15)$$

The contribution fractions allow us to estimate the coercivities of the fractions, taking into consideration the experimental values of H_c and H_{cr}. We will approximately assume that the particles have uniaxial crystallography with K_{ui} constants. Then the magnetization reversal fields of the blocked superparamagnetic H_{i2} [75], single domains H_{i3} [76], and pseudo-single H_{i4} [77] of particles are equal to the following:

$$H_{i2} = H_{i3}\left(1 - \left(\frac{d_{i2}}{d_{i3}}\right)^{3/2}\right),\ H_{i3} = \frac{2K_{ui}}{I_{si}},\ H_{i4} = H_{i3}\frac{d_{i3}}{d_{i4}}. \quad (16)$$

Neglecting the MD contribution of the particles of the first fraction and considering that the third fraction includes only SD particles, we calculate the average magnetization reversal field of the particles of each fraction:

$$H_{0i} = \frac{H_{i2}c_{i2} + H_{i3}c_{i3} + H_{i4}c_{i4}}{c_{i2} + c_{i3} + c_{i4}},\ i = 1,\ 2;\ H_{03} = H_{33} \quad (17)$$

Then it is possible to estimate the magnetization reversal field H_0 and coercive force $H_{c\,est}$ of the sample:

$$H_0 = \sum_i \delta_i H_{0i},\ H_{c\,est} = \frac{H_c}{H_{cr}}H_0. \quad (18)$$

The agreement of H_0 with the experimental value of H_{cr} was carried out by selecting the values of Δ_1 and K_{ui}, which allowed us to additionally justify the preliminary choice of the ranges of the I_{si} values.

We calculate the effective spontaneous magnetizations and estimate the ferrimagnet's concentrations in the samples only at a temperature of 295 K. No modeling was carried out at 2 K, since in this case, an additional fraction with a large saturation magnetization (Table 3) clearly appears, the magnetic properties of which are not precisely known. Moreover, at 2 K, quantum effects are significant, which are not taken into consideration by the macroscopic SDEM model.

As noted earlier (Section 4.5), the *fd* value correlates with the fraction of SP particles in the sample. According to Table 4, the samples contain a significant amount of SP particles. Since the FD factor of the ClayL sample cannot be calculated accurately (Figure 9a), and its M_s and M_{rs} values are significantly lower than those of the other samples, the estimates for it will be of low accuracy. Therefore, only the simulation results for the Lab and Ind samples are presented below.

The parameters of the lognormal particle volume distribution were chosen so that the total fraction of volume concentration of SP particles of both fractions $c_{sp} = c_{11} + c_{21}$ coincided with the value of *fd*: c_{sp} = 0.105 for the Lab sample and c_{sp} = 0.065 for the Ind

sample. Moreover, the average particle size in the samples was d_m = 18 nm for the Lab sample and d_m = 19 nm for the Ind sample.

According to the assumptions made above about the magnetic materials constituting the three fractions (maghemite/non-stoichiometric magnetite, highly coercive similar ε-Fe_2O_3, hematite), the following ranges of the I_{si} and K_{ui} values were chosen: I_{s1} = 400–450 kA/m, I_{s2} = 120 kA/m, I_{s3} = 2 kA/m, K_{u1} = 4–8 kJ/m^3, K_{u2} = 10–12 kJ/m^3, and K_{u3} = 10–12 kJ/m^3. Using the given parameters, theoretical modeling was performed (see Table 5).

Table 5. Results of theoretical modeling. Denotations: Δ_1 is the fraction of low-coercivity fraction (maghemite/non-stoichiometric magnetite), c_f is the volume concentration of ferrimagnet in the sample, $I_{eff\,rs}$ and $I_{eff\,rs1}$ are the effective spontaneous remanent magnetization (total and first fraction), δ_i is the relative contribution of the i-th fraction to M_{rs} of the sample.

Sample	Δ_1, %	c_f, 10^{-3}	$I_{eff\,rs}$, kA/m	$I_{eff\,rs1}$, kA/m	δ_1, %	δ_2, %	δ_3, %
Lab	76–84	0.80–0.93	37–43	33–41	67.4–78.3	31.9–21.2	0.7–0.5
Ind	52–63	0.42–0.50	66–79	82–102	65.8–76.4	33.4–23.0	0.8–0.6

Figure 10 shows examples of calculated values of average magnetization reversal fields for two main fractions (H_{01} and H_{02}) for Lab (Δ_1 = 76%) and Ind (Δ_1 = 52%) samples, depending on the average particle sizes in the corresponding magnetic states (SP, bSP, SD, PSD, and MD).

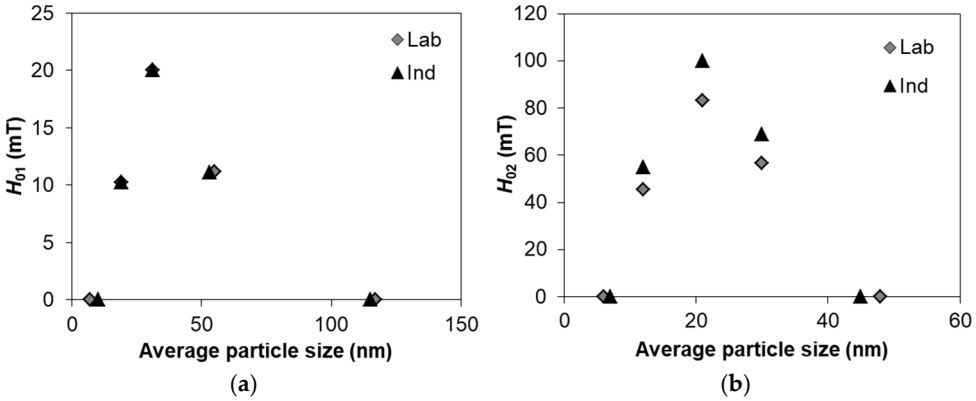


Figure 10. Characteristic dependencies of the magnetization reversal fields of the first (**a**) and second (**b**) fractions on the average particle size in the corresponding magnetic states for Lab and Ind samples.

Despite the fact that, in the initial approximation, the proportion of the first fraction Δ_1 in the Lab and Ind samples differs by more than 20%, the relative contribution of the i-th fraction to M_{rs} (see Table 5) and the magnetization reversal fields are close (see Figure 10). This suggests that in both types of samples, the fractions consist of the same polymorphs of iron (III) oxide: the first fraction is close in composition to γ-Fe_2O_3, and the second fraction is similar to ε-Fe_2O_3.

Figure 4 shows the fracture curves and coercivity spectra of the hysteresis-free remanent magnetization obtained in a constant field H = 0.5 mT. The maximum amplitude of the destructive alternating field is h = 100 mT. The coercivity spectra of the Ind and Lab samples have maxima corresponding to the low-coercivity fraction, but since for both samples H_{cr} is greater than 100 mT, it is clear that the high-coercivity fraction is hardly involved in the creation of ARM. The ARM can be estimated using the approximation of a uniform

distribution of random fields of magnetostatic interaction $W(H_i) = 1/(2H_{i\,max})$, using the following formula [24,25]:

$$M_{ri} = c_r \delta_1 I_s \frac{H}{H_{i\max}} \frac{V}{m} \quad (19)$$

where the multiplier $c_r\delta_1$ takes into consideration the contribution of the low-coercivity fraction particles to the volume concentration of the remanent magnetization (12), the maximum interaction field in our case $H_{i\ \max} \approx 0.5I_s$. For the Lab sample, the experimental value of $M_{ri} = 2.63 \cdot 10^{-3}$ A·m^2/kg, theoretical estimates in the range $M_{ri} = (2.43–2.99) \cdot 10^{-3}$ A·m^2/kg, the best agreement is obtained at $\Delta_1 = 0.82$, $I_{s1} = 450$ kA/m, $\delta_1 = 0.78$ and $c_f = 0.80 \cdot 10^{-3}$. For sample Ind, experimental value of $M_{ri} = 1.17 \cdot 10^{-3}$ A·m^2/kg, theoretical estimates in the range of $M_{ri} = (1.19–1.34) \cdot 10^{-3}$ A·m^2/kg, the best agreement is obtained at $\Delta_1 = 0.52$, $I_{s1} = 450$ kA/m, $\delta_1 = 0.66$ and $c_f = 0.47 \cdot 10^{-3}$.

6. Conclusions

The investigated fired clays have a complex mineralogical composition, which determines their magnetic properties. The complex analysis performed in this work allows us to conclude that these properties are formed due to a microheterogeneous ensemble of magnetic particles, including fractions with different coercivity and spontaneous magnetization with size distribution and magnetic states. Spectrometric and magnetic measurements revealed the presence of a number of features. Presumably, the samples contain iron oxides in various polymorphic modifications, namely maghemite and hematite, as well as a ε-Fe_2O_3-like fraction. In addition, non-stoichiometric magnetite may be present in the samples. The spectrum of possible magnetic states of particles is quite wide: from superparamagnetic to multidomain.

The theoretical analysis based on the model of magnetostatically interacting particles (SDEM) allowed us to quantitatively estimate the distribution of particles into fractions and magnetic states. The coincidence of the calculated and experimental values of the parameters M_s, M_{rs}, H_c, H_{cr}, and M_{ri} confirmed the applicability of the used model. The concentration of ferrimagnet in the samples is small ($c_f < 0.1\%$), and in the Lab sample it is two times higher than in Ind. At the same time, the effective spontaneous magnetizations on the remanent magnetization, which have a value of the order of several tens of kA/m, in the Lab sample, on the contrary, are about two times lower than in Ind. This leads to the fact that, in agreement with the experimental data, the contribution of the considered fractions to the remanent magnetization appears to be approximately the same in both samples: strongly magnetic ~0.75 and weakly magnetic ~0.25.

It should be noted that at a sufficiently low concentration of ferrimagnet in the samples, the concentration of superparamagnetic particles is even two orders of magnitude lower. Nevertheless, the use of pulse methods and the FD factor allows us to diagnose the presence of SP particles more reliably, which in turn makes it possible to reconstruct the distribution of particles by magnetic states and calculate hysteresis characteristics.

Thus, the integrated application of a wide range of experimental methods with theoretical modeling allows us to identify and quantitatively describe the microheterogeneous nature of the magnetic state of baked clays. This approach opens up opportunities for in-depth analysis of the thermal and phase history of archaeological and geological samples and can be applied to a wide range of materials.

Author Contributions: Conceptualization, P.K.; Data curation, P.K., A.R., and E.S.; Formal analysis, P.K., S.Y., A.R., and E.S.; Investigation, A.K., S.Y., N.Z., D.Z., and E.S.; Methodology, P.K., A.R., and E.S.; Project administration, P.K.; Resources, P.K., S.Y., and E.S.; Validation, P.K. and E.S.; Visualization, P.K. and A.R.; Writing—original draft, P.K. and E.S.; Writing—review and editing, A.K., N.B.

(Nadezhda Belskaya), S.Y., K.G., N.B. (Nikita Bobrov), A.R., and N.Z. All authors have read and agreed to the published version of the manuscript.

Funding: This research received no external funding.

Data Availability Statement: The original contributions presented in this study are included in the article. Further inquiries can be directed to the corresponding author(s).

Acknowledgments: Scientific research was performed at the Research Park of St. Petersburg State University: "Center for Diagnostics of Functional Materials for Medicine, Pharmacology and Nanoelectronics"; "Nanotechnologies"; "Geomodel"; "Resource Center for Microscopy and Microanalysis"; "X-ray diffraction methods of research"; "Innovative Technologies of Composite Nanomaterials"; "Chemical Analysis and Materials Research Center". The authors thank the Institute of Precambrian Geology and Geochronology, Russian Academy of Sciences, for conducting the Mössbauer spectroscopy experiments.

Conflicts of Interest: Author Nikita Zolotov was employed by the company SemiTEq JSC. The remaining authors declare that the research was conducted in the absence of any commercial or financial relationships that could be construed as a potential conflict of interest.

References

1. Rancourt, D.G. Magnetism of Earth, Planetary, and Environmental Nanomaterials. *Rev. Mineral. Geochem.* **2001**, *44*, 217–292. [CrossRef]
2. Evans, M.E.; Heller, F. *Environmental Magnetism: Principles and Applications of Enviromagnetics*; Academic Press: San Diego, CA, USA, 2003; ISBN 0122438515.
3. Jordanova, N. *Soil Magnetism: Applications in Pedology, Environmental Science and Agriculture*; Elsevier Science: Amsterdam, The Netherlands, 2016; ISBN 0128092394.
4. Peters, C.; Thompson, R. Supermagnetic Enhancement, Superparamagnetism, and Archaeological Soils. *Geoarchaeology-An Int. J.* **1999**, *14*, 401–413. [CrossRef]
5. Chen, G.; Li, G.; Liu, M.; Ge, W.; Wu, G.; Zhan, C. The Firing Temperatures of Burnt Clay from the Chinese Neolithic Cultural Relics and Its Paleoenvironmental Imprints. *Heliyon* **2023**, *9*, e20628. [CrossRef] [PubMed]
6. Jordanova, N.; Jordanova, D.; Kostadinova-Avramova, M. Synergy of Environmental Magnetism and Archaeomagnetism for the Benefit of Archaeology—State of the Art in Bulgaria. In *World Archaeo-Geophysics*; Springer: Cham, Switzerland, 2024. [CrossRef]
7. Maher, B.A. Palaeoclimatic Records of the Loess/Palaeosol Sequences of the Chinese Loess Plateau. *Quat. Sci. Rev.* **2016**, *154*, 23–84. [CrossRef]
8. Kermenidou, M.; Balcells, L.; Martinez-Boubeta, C.; Chatziavramidis, A.; Konstantinidis, I.; Samaras, T.; Sarigiannis, D.; Simeonidis, K. Magnetic Nanoparticles: An Indicator of Health Risks Related to Anthropogenic Airborne Particulate Matter. *Environ. Pollut.* **2021**, *271*, 116309. [CrossRef]
9. Néel, L. Théorie Du Traînage Magnétique Des Ferromagnétiques En Grains Fins Avec Application Aux Terres Cuites. *Ann. Geophys.* **1949**, *5*, 99–136.
10. Kharitonskiĭ, P.V. Magnetostatic Interaction of Superparamagnetic Particles Dispersed in a Thin Layer. *Phys. Solid State* **1997**, *39*, 162–163. [CrossRef]
11. Kharitonskii, P.V.; Gareev, K.G.; Ionin, S.A.; Ryzhov, V.A.; Bogachev, Y.V.; Klimenkov, B.D.; Kononova, I.E.; Moshnikov, V.A. Microstructure and Magnetic State of Fe_3O_4-SiO_2 Colloidal Particles. *J. Magn.* **2015**, *20*, 221–228. [CrossRef]
12. Barsukov, P.; Soupios, P.; Gorokhovich, Y. Application of Special SPM Loop in Archaeological Prospection. In Proceedings of the 20th International Geophysical Congress and Exhibition of Turkey, Antalya, Turkey, 25–27 November 2013; pp. 90–93.
13. Kozhevnikov, N.O.; Antonov, E.Y. Aftereffects in the Transient Electromagnetic Method: Magnetic Viscosity. *Russ. Geol. Geophys.* **2022**, *63*, 312–320. [CrossRef]
14. Cowan, D.C.; Song, L.P.; Oldenburg, D.W. Transient VRM Response From a Large Circular Loop Over a Conductive and Magnetically Viscous Half-Space. *IEEE Trans. Geosci. Remote Sens.* **2017**, *55*, 3669–3678. [CrossRef]
15. Barsukov, P.O.; Fainberg, E.B. Study of the Environment by the Transient Electromagnetic Method Using the Induced Polarization and Superparamagnetic Effects. *Izv. Phys. Solid Earth* **2002**, *38*, 981–984.
16. Thiesson, J.; Tabbagh, A.; Flageul, S. TDEM Magnetic Viscosity Prospecting Using a Slingram Coil Configuration. *Near Surf. Geophys.* **2007**, *5*, 363–374. [CrossRef]
17. McNeill, J.D. *The Magnetic Susceptibility of Soils Is Definitely Complex*; Technical Note TN-36; Geonix Limited: London, UK, 2013; 27p.

18. Finco, C.; Rejiba, F.; Schamper, C.; Cavalcante Fraga, L.H.; Wang, A. Calibration of near-surface multi-frequency electromagnetic induction data. *Geophys. Prospect.* **2023**, *71*, 765–779. [CrossRef]
19. Kozhevnikov, N.O.; Kharinsky, A.V.; Kozhevnikov, O.K. An Accidental Geophysical Discovery of an Iron Age Archaeological Site on the Western Shore of Lake Baikal. *J. Appl. Geophys.* **2001**, *47*, 107–122. [CrossRef]
20. Faivre, D. *Iron Oxides: From Nature to Applications*; Wiley: Hoboken, NJ, USA, 2016; ISBN 9783527691395. [CrossRef]
21. Machala, L.; Tuček, J.; Zbořil, R. Polymorphous Transformations of Nanometric Iron(III) Oxide: A Review. *Chem. Mater.* **2011**, *23*, 3255–3272. [CrossRef]
22. Jeong, J.H.; Kim, H.H.; Lee, J.G.; Baek, Y.K. Epsilon Iron Oxide (ε-Fe_2O_3) as an Electromagnetic Functional Material: Properties, Synthesis, and Applications. *J. Powder Mater.* **2024**, *31*, 465–479. [CrossRef]
23. Kharitonskii, P.; Kamzin, A.; Gareev, K.; Valiullin, A.; Vezo, O.; Sergienko, E.; Korolev, D.; Kosterov, A.; Lebedev, S.; Gurylev, A.; et al. Magnetic Granulometry and Mössbauer Spectroscopy of Fe_mO_n–SiO_2 Colloidal Nanoparticles. *J. Magn. Magn. Mater.* **2018**, *461*, 30–36. [CrossRef]
24. Gurylev, A.; Kharitonskii, P.; Kosterov, A.; Berestnev, I.; Sergienko, E. Magnetic Properties of Fired Clay (Bricks) Possibly Containing Epsilon Iron (III) Oxide. *J. Phys. Conf. Ser.* **2019**, *1347*, 012034. [CrossRef]
25. Kharitonskii, P.; Bobrov, N.; Gareev, K.; Kosterov, A.; Nikitin, A.; Ralin, A.; Sergienko, E.; Testov, O.; Ustinov, A.; Zolotov, N. Magnetic Granulometry, Frequency-Dependent Susceptibility and Magnetic States of Particles of Magnetite Ore from the Kovdor Deposit. *J. Magn. Magn. Mater.* **2022**, *553*, 169279. [CrossRef]
26. Bobrov, N.; Sergienko, E.; Yanson, S.; Kosterov, A.; Karpinsky, V.; Kharitonskii, P.; Ralin, A. Magnetic Viscosity of Suevites from the Zhamanshin Impact Crater. In *Problems of Geocosmos—2022*; Springer Proceedings in Earth and Environmental Sciences; Springer: Berlin/Heidelberg, Germany, 2023; Volume 2023, pp. 85–109. [CrossRef]
27. Kharitonskii, P.; Sergienko, E.; Ralin, A.; Setrov, E.; Sheidaev, T.; Gareev, K.; Ustinov, A.; Zolotov, N.; Yanson, S.; Dubeshko, D. Superparamagnetism of Artificial Glasses Based on Rocks: Experimental Data and Theoretical Modeling. *Magnetochemistry* **2023**, *9*, 220. [CrossRef]
28. Doebelin, N.; Kleeberg, R. Profex: A Graphical User Interface for the Rietveld Refinement Program BGMN. *J. Appl. Crystallogr.* **2015**, *48*, 1573–1580. [CrossRef] [PubMed]
29. Lowrie, W. Identification of Ferromagnetic Minerals in a Rock by Coercivity and Unblocking Temperature Properties. *Geophys. Res. Lett.* **1990**, *17*, 159–162. [CrossRef]
30. Applied Electromagnetic Research. Applied Electromagnetic Research. Available online: http://www.aemr.net/ (accessed on 4 March 2025).
31. Kharitonskii, P.V.; Setrov, E.A.; Ralin, A.Y. Modeling of Hysteresis Characteristics of a Dilute Magnetic with Dipole-Dipole Interaction of Particles. *Mater. Phys. Mech.* **2024**, *52*, 142–150. [CrossRef]
32. Abert, C. Micromagnetics and Spintronics: Models and Numerical Methods. *Eur. Phys. J. B* **2019**, *92*, 120. [CrossRef]
33. Leliaert, J.; Mulkers, J. Tomorrow's Micromagnetic Simulations. *J. Appl. Phys.* **2019**, *125*, 180901. [CrossRef]
34. Donnelly, C.; Hierro-Rodríguez, A.; Abert, C.; Witte, K.; Skoric, L.; Sanz-Hernández, D.; Finizio, S.; Meng, F.; McVitie, S.; Raabe, J.; et al. Complex Free-Space Magnetic Field Textures Induced by Three-Dimensional Magnetic Nanostructures. *Nat. Nanotechnol.* **2022**, *17*, 136–142. [CrossRef]
35. Kharitonskii, P.; Zolotov, N.; Kirillova, S.; Gareev, K.; Kosterov, A.; Sergienko, E.; Yanson, S.; Ustinov, A.; Ralin, A. Magnetic Granulometry, Mössbauer Spectroscopy, and Theoretical Modeling of Magnetic States of FemOn–Fem-XTixOn Composites. *Chin. J. Phys.* **2022**, *78*, 271–296. [CrossRef]
36. Olin, M.; Anttila, T.; Dal Maso, M. Using a Combined Power Law and Log-Normal Distribution Model to Simulate Particle Formation and Growth in a Mobile Aerosol Chamber. *Atmos. Chem. Phys.* **2016**, *16*, 7067–7090. [CrossRef]
37. Fujihara, A.; Tanimoto, S.; Yamamoto, H.; Ohtsuki, T. Log-Normal Distribution in a Growing System with Weighted and Multiplicatively Interacting Particles. *J. Phys. Soc. Japan* **2018**, *87*, 034001. [CrossRef]
38. Hrouda, F. Models of Frequency-Dependent Susceptibility of Rocks and Soils Revisited and Broadened. *Geophys. J. Int.* **2011**, *187*, 1259–1269. [CrossRef]
39. Kostadinova-Avramova, M.; Kovacheva, M. The Magnetic Properties of Baked Clays and Their Implications for Past Geomagnetic Field Intensity Determinations. *Geophys. J. Int.* **2013**, *195*, 1534–1550. [CrossRef]
40. Putnis, A.; McConnell, J.D.C. *Principles of Mineral Behaviour*; Blackwell Scientific Publications: Oxford, UK, 1980; 257p.
41. Murad, E.; Wagner, U. The Mössbauer Spectrum of Illite. *Clay Miner.* **1994**, *29*, 1–10. [CrossRef]
42. López-Sánchez, J.; Palencia-Ortas, A.; del Campo, A.; McIntosh, G.; Kovacheva, M.; Martín-Hernández, F.; Carmona, N.; Rodríguez de la Fuente, O.; Marín, P.; Molina-Cardín, A.; et al. Further Progress in the Study of Epsilon Iron Oxide in Archaeological Baked Clays. *Phys. Earth Planet. Inter.* **2020**, *307*, 106554. [CrossRef]
43. McIntosh, G.; Kovacheva, M.; Catanzariti, G.; Donadini, F.; Lopez, M.L.O. High Coercivity Remanence in Baked Clay Materials Used in Archeomagnetism. *Geochem. Geophys. Geosystems* **2011**, *12*, 1–17. [CrossRef]

44. Kosterov, A.; Kovacheva, M.; Kostadinova-Avramova, M.; Minaev, P.; Salnaia, N.; Surovitskii, L.; Yanson, S.; Sergienko, E.; Kharitonskii, P. High-Coercivity Magnetic Minerals in Archaeological Baked Clay and Bricks. *Geophys. J. Int.* **2021**, *224*, 1256–1271. [CrossRef]
45. Vandenberghe, R.E.; De Grave, E. Application of Mössbauer Spectroscopy in Earth Sciences. In *Mössbauer Spectroscopy*; Springer: Berlin/Heidelberg, Germany, 2013; pp. 91–185.
46. Maher, B.A.; Ahmed, I.A.M.; Karloukovski, V.; MacLaren, D.A.; Foulds, P.G.; Allsop, D.; Mann, D.M.A.; Torres-Jardón, R.; Calderon-Garciduenas, L. Magnetite Pollution Nanoparticles in the Human Brain. *Proc. Natl. Acad. Sci. USA* **2016**, *113*, 10797–10801. [CrossRef]
47. Shokanov, A.; Manakova, I.; Vereshchak, M.; Migunova, A. Characterization of Kazakhstan's Clays by Mössbauer Spectroscopy and X-ray Diffraction. *Minerals* **2024**, *14*, 713. [CrossRef]
48. Tuček, J.; Zbořil, R.; Namai, A.; Ohkoshi, S.I. ε-Fe_2O_3: An Advanced Nanomaterial Exhibiting Giant Coercive Field, Millimeter-Wave Ferromagnetic Resonance, and Magnetoelectric Coupling. *Chem. Mater.* **2010**, *22*, 6483–6505. [CrossRef]
49. López-Sánchez, J.; McIntosh, G.; Osete, M.L.; del Campo, A.; Villalaín, J.J.; Pérez, L.; Kovacheva, M.; Rodríguez de la Fuente, O. Epsilon Iron Oxide: Origin of the High Coercivity Stable Low Curie Temperature Magnetic Phase Found in Heated Archeological Materials. *Geochem. Geophys. Geosystems* **2017**, *18*, 2646–2656. [CrossRef]
50. Thompson, R.; Oldfield, F. *Environmental Magnetism*; Springer: Dordrecht, Germany, 2012; ISBN 978-94-011-8038-2.
51. Nogués, J.; Sort, J.; Langlais, V.; Doppiu, S.; Dieny, B.; Muñoz, J.S.; Suriñach, S.; Baró, M.D.; Stoyanov, S.; Zhang, Y. Exchange Bias in Ferromagnetic Nanoparticles Embedded in an Antiferromagnetic Matrix. *Int. J. Nanotechnol.* **2005**, *2*, 23–42. [CrossRef]
52. López-Ortega, A.; Estrader, M.; Salazar-Alvarez, G.; Roca, A.G.; Nogués, J. Applications of Exchange Coupled Bi-Magnetic Hard/Soft and Soft/Hard Magnetic Core/Shell Nanoparticles. *Phys. Rep.* **2015**, *553*, 1–32. [CrossRef]
53. Balaev, D.A.; Krasikov, A.A.; Dubrovskiy, A.A.; Popkov, S.I.; Stolyar, S.V.; Iskhakov, R.S.; Ladygina, V.P.; Yaroslavtsev, R.N. Exchange Bias in Nano-Ferrihydrite. *J. Appl. Phys.* **2016**, *120*, 183903. [CrossRef]
54. Thi, T.N.; Van, P.C.; Artavazd, K.; Hwang, C.; Choi, J.; Kim, H.; Jeong, J.R. Effect of Heat-Treatment Temperature on the Formation of ε-Fe_2O_3 Nanoparticles Encapsulated by SiO_2. *J. Magn.* **2023**, *28*, 239–244. [CrossRef]
55. Tauxe, L.; Mullender, T.A.T.; Pick, T. Potbellies, Wasp-Waists, and Superparamagnetism in Magnetic Hysteresis. *J. Geophys. Res. Solid Earth* **1996**, *101*, 571–583. [CrossRef]
56. Özdemir, Ö.; Dunlop, D.J. Hysteresis and Coercivity of Hematite. *J. Geophys. Res. Solid Earth* **2014**, *119*, B02101. [CrossRef]
57. Roberts, A.P.; Cui, Y.; Verosub, K.L. Wasp-Waisted Hysteresis Loops: Mineral Magnetic Characteristics and Discrimination of Components in Mixed Magnetic Systems. *J. Geophys. Res.* **1995**, *100*, 17909–17924. [CrossRef]
58. Dunlop, D.J. Theory and application of the Day plot (M_{rs}/M_s versus H_{cr}/H_c) 2. Application to data for rocks, sediments, and soils. *J. Geophys. Res. Solid Earth* **2002**, *107*, EPM 5-1–EPM 5-15. [CrossRef]
59. Fabian, K. Some Additional Parameters to Estimate Domain State from Isothermal Magnetization Measurements. *Earth Planet. Sci. Lett.* **2003**, *213*, 337–345. [CrossRef]
60. Muxworthy, A.R.; Williams, W. Critical Superparamagnetic/Single-Domain Grain Sizes in Interacting Magnetite Particles: Implications for Magnetosome Crystals. *J. R. Soc. Interface* **2009**, *6*, 1207–1212. [CrossRef] [PubMed]
61. Liu, Q.; Roberts, A.P.; Torrent, J.; Horng, C.S.; Larrasoaña, J.C. What Do the HIRM and S-Ratio Really Measure in Environmental Magnetism? *Geochem. Geophys. Geosystems* **2007**, *8*, 1–10. [CrossRef]
62. Gehring, A.U.; Fischer, H.; Louvel, M.; Kunze, K.; Weidler, P.G. High Temperature Stability of Natural Maghemite: A Magnetic and Spectroscopic Study. *Geophys. J. Int.* **2009**, *179*, 1361–1371. [CrossRef]
63. Dunlop, D.J.; Özdemir, Ö. *Rock Magnetism. Fundamentals and Frontiers. Cambridge Studies in Magnetism Series*; Cambridge University Press: Cambridge, UK, 1997; ISBN 978-0521000987.
64. Özdemir, Ö.; Banerjee, S.K. High Temperature Stability of Maghemite (γ-Fe_2O_3). *Geophys. Res. Lett.* **1984**, *11*, 161–164. [CrossRef]
65. Moskowitz, B.M.; Frankel, R.B.; Bazylinski, D.A. Rock Magnetic Criteria for the Detection of Biogenic Magnetite. *Earth Planet. Sci. Lett.* **1993**, *120*, 283–300. [CrossRef]
66. Housen, B.A.; Banerjee, S.K.; Moskowitz, B.M. Low-Temperature Magnetic Properties of Siderite and Magnetite in Marine Sediments. *Geophys. Res. Lett.* **1996**, *23*, 2843–2846. [CrossRef]
67. Smirnov, A.V.; Tarduno, J.A. Low-Temperature Magnetic Properties of Pelagic Sediments (Ocean Drilling Program Site 805C): Tracers of Maghemitization and Magnetic Mineral Reduction. *J. Geophys. Res. Solid Earth* **2000**, *105*, 16457–16471. [CrossRef]
68. Özdemir, Ö.; Dunlop, D.J. Hallmarks of Maghemitization in Low-Temperature Remanence Cycling of Partially Oxidized Magnetite Nanoparticles. *J. Geophys. Res.* **2010**, *115*, B02101. [CrossRef]
69. Dearing, J.A.; Dann, R.J.L.; Hay, K.; Lees, J.A.; Loveland, P.J.; Maher, B.A.; O'Grady, K. Frequency-Dependent Susceptibility Measurements of Environmental Materials. *Geophys. J. Int.* **1996**, *124*, 228–240. [CrossRef]
70. Khurshid, H.; Lampen-Kelley, P.; Iglesias, Ò.; Alonso, J.; Phan, M.H.; Sun, C.J.; Saboungi, M.L.; Srikanth, H. Spin-Glass-like Freezing of Inner and Outer Surface Layers in Hollow γ-Fe_2O_3 Nanoparticles. *Sci. Rep.* **2015**, *5*, 15054. [CrossRef]

71. Mugiraneza, S.; Hallas, A.M. Tutorial: A Beginner's Guide to Interpreting Magnetic Susceptibility Data with the Curie-Weiss Law. *Commun. Phys.* **2022**, *5*, 1–12. [CrossRef]
72. Kumar, P.; Gupta, P. Halloysite-Based Magnetic Nanostructures for Diverse Applications: A Review. *ACS Appl. Nano Mater.* **2023**, *6*, 13824–13868. [CrossRef]
73. Balaev, D.A.; Semenov, S.V.; Dubrovskiy, A.A.; Knyazev, Y.V.; Kirillov, V.L.; Shaykhutdinov, K.A.; Martyanov, O.N. Size Effect and Temperature of Magnetic Ordering in ε-Fe_2O_3 Nanoparticles. *J. Supercond. Nov. Magn.* **2025**, *38*, 184. [CrossRef]
74. Sakurai, S.; Namai, A.; Hashimoto, K.; Ohkoshi, S. First Observation of Phase Transformation of All Four Fe_2O_3 Phases ($\gamma \rightarrow \varepsilon \rightarrow \beta \rightarrow \alpha$-Phase). *J. Am. Chem. Soc.* **2009**, *131*, 18299–18303. [CrossRef] [PubMed]
75. Kneller, E.F.; Luborsky, F.E. Particle Size Dependence of Coercivity and Remanence of Single-Domain Particles. *J. Appl. Phys.* **1963**, *34*, 656–658. [CrossRef]
76. Stoner, E.C.; Wohlfarth, E.P. A Mechanism of Magnetic Hysteresis in Heterogeneous Alloys. *Philos. Trans. R. Soc. London. Ser. A, Math. Phys. Sci.* **1948**, *240*, 599–642. [CrossRef]
77. Roberts, A.P.; Almeida, T.P.; Church, N.S.; Harrison, R.J.; Heslop, D.; Li, Y.; Li, J.; Muxworthy, A.R.; Williams, W.; Zhao, X. Resolving the Origin of Pseudo-Single Domain Magnetic Behavior. *J. Geophys. Res. Solid Earth* **2017**, *122*, 9534–9558. [CrossRef]

Disclaimer/Publisher's Note: The statements, opinions and data contained in all publications are solely those of the individual author(s) and contributor(s) and not of MDPI and/or the editor(s). MDPI and/or the editor(s) disclaim responsibility for any injury to people or property resulting from any ideas, methods, instructions or products referred to in the content.